Enhanced phonon-plasmon interaction in film-coupled dimer nanoridges mediated by surface acoustic waves

Adnane Noual, Rock Akiki, Gaëtan Lévêque, Yan Pennec, Bahram Djafari-Rouhani

Research Article | Vol. 29, No. 26 / 20 Dec 2021 / Optics Express 43104
Optics EXPRESS

Enhanced phonon-plasmon interaction in film-coupled dimer nanoridges mediated by surface acoustic waves

A. NOUAL,[1,2,*] R. AKIKI,[1] G. LÉVÊQUE,[2] Y. PENNEC,[2] AND B. DJAFARI-ROUHANI[2]

[1]LPMR, Département de Physique, Faculté des Sciences, Université Mohamed Premier, 60000 Oujda, Morocco
[2]IEMN, UMR CNRS 8520, Département de Physique, Université de Lille, 59655 Villeneuve d'Ascq, France
[*]a.noual@gmail.ac.ma

Abstract: The interaction between phonons and localized plasmons in coupled nanoparticles can be exploited both for modulating the scattered electromagnetic field and the understanding of the mechanical vibrations at nanoscale. In this paper, we demonstrate by numerical analysis an enhanced optomechanical interaction in a film-coupled gold dimer nanoparticles mediated by surface acoustic waves. Two gold nanoridges are placed atop a multilayer structure consisting of a thin dielectric spacer covering a gold film layer on a silicon dioxide substrate. Numerical simulations of the optical properties reveal the existence of three surface localized plasmons in the infrared range with enhanced scattering and narrower linewidths than with a single nanoridge. The physical origin of such modes as well as their tunability as function of key geometrical parameters are successfully captured with a simple model based on effective Metal-Insulator-Metal (MIM)-like plasmonic cavity. We calculate the optomechanic coupling rates between the GHz localized mechanical modes and plasmonic modes of the dimer, finding that the strongest coupling is observed for the in-phase compressional mode followed by the out-of-phase flexural mode. Both such modes can be excited by launching a surface acoustic wave (Sezawa wave) at the inlet in front of the dimer structure. It is also found that the flexural mode which is inactive optomechanically in case of a monomer becomes active due to dimer coupling, with a significant phonon-plasmon coupling rate. The findings in this work may facilitate design of new optomechanical components monitored with fast coherent acoustics, leading to new generation of light acousto-optic modulators where strong optomechanical interactions are required.

1. Introduction

Nano/micro-opto mechanical devices have gained a substantial interest lately due to their capacity of controlling the flow of light in nanoscale photonic structures [1,2] and to the potential practical applications they offer in terms of ultra-sensitive mass [3] or charge measurements [4,5]. Such components are also shown to provide utility in fundamental physics as in quantum information processing and control and/or enhancement of light-mater interaction [6–8]. The light sound coupling can be described by two physical mechanisms which are both based on a local variation of the dielectric constant namely, a volume photoelastic effect [9,10] consisting in the local modulation of the dielectric constant of the material by the phonon induced strain field, and a surface effect resulting from the deformations of the interfaces/boundaries that separate two adjacent media, referred to as moving-boundary effect [11,12]. A special class of optomechanical structures which enable to achieve strong light-sound interactions is based on cavities created in the so-called phoxonic crystals [13]. The strong optomechanical coupling (OMC) is mainly due to the photons and phonons band gaps exhibited by such crystal cavities, resulting in simultaneous highly localized light and sound which in turn gives rise to enhanced OMC. Intense efforts have

#444430 https://doi.org/10.1364/OE.444430
Journal © 2021 Received 28 Sep 2021; revised 8 Nov 2021; accepted 25 Nov 2021; published 9 Dec 2021

Optics EXPRESS

been put lately to investigate strong OMC in these systems as in triangularly shaped phoxonic cavities [14], nanobeams [15–18] and in phoxonic-plasmonic cavities based on metal strips [19].

On the other hand, localized surface plasmon (LSP) supported by small metallic nanoparticles has been exploited due to the extreme field enhancement they manifest to study nanoscale mechanical oscillations of such systems, generally through the use of Brillouin/Raman light spectroscopy. In these set-ups, the LSP interacts with the localized phonons in the nanoparticles, giving rise to enhanced inelastic light scattering which reveals the particles mechanical eigenmodes such as in [20–22], where single gold dimers or ensemble silver dimers in polymer matrices acoustic modes have been fully characterized. Another experimental means harnessing acousto-plasmonic coupling to study nanoscale mechanical vibrations is the ultrafast pump-probe technique where the plasmonic absorption/transmission is temporally monitored, uncovering as a result the nanostructures eigenmodes [23–25]. Besides, a specific surface plasmon type mode has attracted much of interest recently due to its exquisite properties particularly in terms of enhanced localized large fields: such strongly confined plasmon arises out of coupling between nanoparticles and their image on a metallic film lying underneath a dielectric nanogap [26–28]. This system is often referred to as metal film-coupled nanoparticles (FCN), and is shown to enable promising applications as plasmon-mediated optical sensing [29], but also the possibility of exploring fundamental quantum physical phenomena [30,31].

In the context of OMC, LSP modes are shown to significantly enhance light-sound interaction [32–34], but due to the ultra-confined plasmonic modes with even larger fields concentrations exhibited by FCN-based structures, stronger OMC can be achieved with a view to better study nanoscale mechanical vibrations [35]. FCN-systems with dimers/trimers atop the metal film instead of monomers are expected to show more interesting features in terms of narrower plasmons linewidth, enhanced associated scattered intensity [28] and new applications [36,37]. It follows that stronger OMC may be attained exploring dimers (or trimers) based FCN systems with a view to applications opportunities as for analysing nanoscale vibrations due to the much stronger fields. Lately, OMC in a FCN design with a gold monomer sitting on top of a gold film has been investigated numerically [38]. Moreover, employment of surface acoustic waves (SAW)-based platforms aiming at monitoring such strong/enhanced OMC is quite desirable due to the nowadays available experimental techniques for the fabrication of such devices. As a matter of fact, high frequency (~GHz range) SAW with sufficiently high amplitude can be readily generated using IDTs (InterDigital Transducers) [39,40] or pulsed laser beams [41]. Recently, enhanced Anti-Stokes scattering within an optomechanical cavity realized on a SAW-based structure has been shown [42], while coherent coupling between high frequency localized phonons and infrared (~ 1.55 μm) photons has been demonstrated using GHz range SAW [43]. Lin et al. have achieved strong OMC in hybrid photonic-plasmonic crystal nanocavities using SAW as a mean of modulating confined photonic-plasmon mode [44]. Also, Korovin et al. showed efficient conversion between IDTs-induced SAW and guided Lamb modes of a nanobeam which transports energy to the optomechanical cavity where OMC can take place [45], whilst strong OMC has been showcased through the use of SAW in a FCN-based geometry with a gold nanocylinder monomer atop a polymer spacer and gold metallic film [46]. However, reports showing enhanced OMC using dimers-based (instead of monomers) FCN structures, much less with the employment of high frequency SAW-platforms intended at controlling such stronger OMC are actually still lacking. This is despite the potential applications that may arise out of enhanced OMC including in the domain of fundamental physics [44] or for studying nano-objects vibrations [47] or so-called plasmonic-like molecules mechanical modes [48]. In addition, the utilization of SAWs with high amplitudes (~ *nm*) enables to significantly enhance the vibration amplitudes of the localized phonons in the dimer nanoparticles, hence increasing the plasmon modulation [44,46]. Such enhanced interactions could lead to much improved Raman/Brillouin scattered signals when studying (dimer) metallic nanoparticles acoustic modes for instance. Also,

Optics EXPRESS

optical excitation of the dimer localized plasmons can be harnessed in detecting SAW with amplitudes as small as a few pm [24] using ultrafast pump-probe technique, making it possible to conceive nanoscale mechanical ultrasensitive high frequency sensors as shown in [49].

In this work, we propose high frequency SAW to investigate enhanced OMC in a dimer-based FCN geometry design. Thorough numerical simulations are performed in order to study optical and mechanical properties of gold ridges dimer sitting atop a polymer spacer under which a thick gold metal film lies over an SiO2 substrate. The dimer coupling gives rise to metal-dielectric-metal-like localized surface plasmons (MIM-LSP) which are confined within the spacer underneath the ridge acting as an effective MIM-cavity, or both underneath and in between such ridges. These MIM-LSP modes are set to lie mostly within the infrared frequency range, and show quite narrower linewidths and stronger scattering intensities comparing with a monomer ridge atop the FCN which is similar to the finding in [28]. Their behaviour with respect to key geometrical parameters is fully captured with a simple effective MIM-cavity model. Mechanical coupling of the dimer leads to the split of their eigen-mechanical modes, resulting in interesting modes which can potentially couple with the plasmons. This interaction is quantitatively evaluated through the computation of optomechanical coefficients, g_{OM}. Then, we analyze surface acoustic waves interaction with the MIM-LSP modes of interest situated at $\sim$ 1638 nm (infrared) and at $\sim$ 926 nm (near infrared). The excitation of the dimer localized phonons via propagative SAW leads to the strong modulation of the MIM-LSP modes. It is found that dimer ridges in-phase compression mechanical mode yields the strongest OMC rate, followed by the out-of-phase flexural mode. The latter mode optomechanically inactive in case of a monomer is shown to become active due to dimer coupling. The findings in this contribution could facilitate the realization of SAW-based devices aimed at the design of ultrasensitive photoacoustic sensors [50], acousto-optic modulators [51] or plasmon-enhanced Raman scattering components [52–54].

2. Dimer optical properties

A sketch of the proposed dimer-FCN geometry design is showed in Fig. 1(a); it is made out of gold metal film lying underneath a polymer dielectric acting as a spacer over which a gold ridge dimer is sitting. The metal film is deposited on a SiO_2 semi-infinite substrate. Due to symmetry invariance of the structure along $y-$axis, we perform all investigations in 2D inside a cross section of the design. The modeled cross section is depicted in Fig. 1(b), where we have surrounded the simulation domain with perfect matched layers (PMLs) in order to prevent undesired reflections. The key geometrical parameters (Fig. 1(b)) are the ridges width D_{Au}, height h_{Au}, inter-dimer separation distance d_{dmr} and the polymer film thickness e_{pol}. Throughout the paper, we chose the gold metal film thickness to be set as 100 nm. The optical skin depth of gold in the optical/infrared range is in the order of $\sim$ 25 nm which makes it possible not to include SiO_2 substrate in the optical scattering simulations as the field would be fully absorbed/reflected before reaching the latter. Materials refractive indices are $n_p \approx 1.5$ for the polymer and $n_{sio2} = 1.46$ for SiO_2, while for the gold material a Lorentz-Drude model is adopted [55,56]. In order to find all the possible modes of the dimer in the frequency range of interest, [600 nm – 2000 nm], we launch the excitation light-wave at oblique incidence (Fig. 1(a)). It is worth mentioning that numerical simulations are carried out here in the frequency domain using Finite Element Method with Comsol Multiphysics Package.

In Fig. 1(c), we show simulations results in terms of scattering spectrum versus wavelength and incidence angle θ for $D_{Au} = 320$ nm, $h_{Au} = 300$ nm, $e_{pol} = 50$ nm and $d_{dmr} = 50$ nm. At an angle of incidence $\theta \gtrsim 51°$, three main modes are observed where scattering (per unit length) increases at roughly $\lambda_1 \approx 1638$ nm (mode p1), $\lambda_2 \approx 926$ nm (mode p2) and $\lambda_3 \approx 628$ nm (mode p3). Actually, these modes correspond to scattering bands rather than sharp peaks due to losses in the metal (increasing FWHM). One notes also a strong excited scattering band towards normal incidence at $\sim$ 1450 nm, but with a quite bigger FWHM comparing with the modes p1, p2 and

Optics EXPRESS

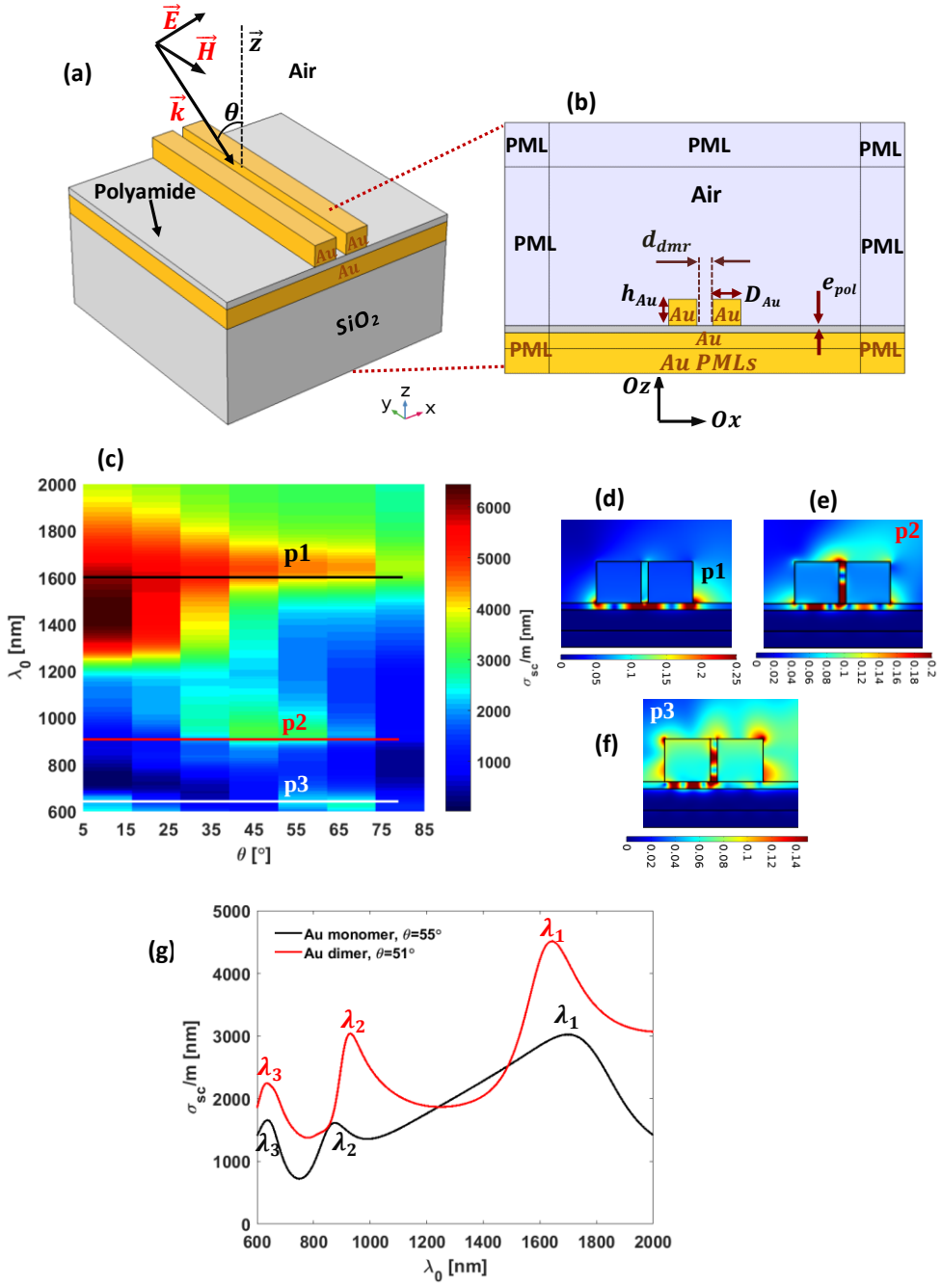

Fig. 1. (a) Schematic diagram of the proposed dimer-based FCN design. Incoming light-wave at oblique incidence is also illustrated. (b) Cross-section of the system depicted in (a) in a *ozx*-cut plane; all key geometrical parameters of the structure are indicated. Perfect matched layers surrounding the structure are employed to avoid unwanted reflections. (c) Simulated extinction spectrum of the geometry sketched in Fig. 1(b) versus wavelength and incoming light incidence angle. (d)-(f) Scattered field map norm within and around the dimer, at $\lambda_1 \approx 1638\ nm$, $\lambda_2 \approx 926\ nm$ and $\lambda_3 \approx 628\ nm$ for an incidence angle of $\theta \approx 51°$; the modes positions are referred to as p1, p2 and p3 in (c). (g) Extinction spectrum for the gold dimer as a function of wavelength for $\theta \approx 51°$ (red line), compared to the case of a gold ridge monomer sitting on the structure sketched in (b) (black line).

Optics EXPRESS

p3 for $\theta \gtrsim 51°$. We shall focus mainly on these latter well-defined modes (at $\theta \sim 51°$), which are potentially useful for the purpose of optomechanical interactions. We observe that mode p1 is effectively excited for $\theta \in [\sim 25° - \sim 75°]$ while modes p2 and p3 are excited in the range of $\theta \in [\sim 25° - \sim 65°]$ and $\theta \in [\sim 45° - \sim 69°]$, respectively. To better interpret such modes, we performed an eigen-frequency quasi normal mode [57] (optical modes with complex frequencies due to absorption in metal) study, where we searched for modes around λ_1, λ_2 and λ_3. The found eigenmodes are overlaid with the scattering spectrum with a black line for the mode p1, a red line for the mode p2 and a white line for the mode p3. A good match is noted taking into account the large FWHM of the modes hindering the determination of their exact positions in the frequency domain. Scattered E_s-field norm map near and around the dimer is shown in Fig. 1(d, e, f) at $\lambda_1 \approx 1638\ nm$ $\lambda_2 \approx 926\ nm$ and $\lambda_3 \approx 628\ nm$, respectively, for an incidence angle $\theta = 51°$. It can be seen that mode p1 is a MIM-type localized surface plasmon strongly confined in the space underneath the ridges acting as an effective MIM-cavity [38]; mode p2 is a higher order MIM-LSP beneath the dimer but with an important MIM-like component confined vertically between the ridges. Mode p3 on the other hand is a higher order MIM-LSP mode under the dimer with higher order vertically confined MIM-like component between ridges. Moreover, modes p2 and particularly mode p3 have antenna-like components associated with multipolar localizations at the edges. Overall, the three modes arise out of coupling of the two ridges, leading to new type of localizations. It should be noted that a weak part of the field of such modes can be scattered into propagative surface plasmon polaritons (SPPs) modes of the multilayer structure while the most part stay localized under and/or in-between the ridges as can be seen from the maps in Fig. 1(d, e, f).

On the other hand, based on the absorption cross section of the dimer versus λ_0 and θ in Supplement 1 (Figs. S1(a)), modes p1, p2 and p3 are non-dispersive as their wavelengths do not change with θ, but their excitation efficiency depend on the latter. We attribute this to the fact that mode p1 is symmetric with respect to median plane ozy of the dimer according to its surface charge density (see Fig. S1(b)) and cannot then be excited at $\theta = 0°$ by the antisymmetric incident light. Modes p2 and p3 are antisymmetric (Figs. S1(c)-S1(d)), meaning they can be excited at $\theta \approx 0°$, but their MIM-component confined under the ridges require probably an important E_z (their main transverse component) i.e., a bigger θ to be excited; when this is realized modes p2 and p3 can be excited. The spectrum shows other modes named as p12, p22 and p32 (see Figs. S1(a)), that result along with p1, p2 and p3 from hybridization of the single ridges modes. Nonetheless, such modes are not very well excited/defined or have a much bigger FWHM, and thus are not useful for our optomechanical coupling purposes.

It is worth mentioning that the equivalent modes to modes p1, p2 and p3 corresponding to the case of a monomer fall at slightly different frequency positions comparing with the dimer (due to dimer coupling), but more importantly they exhibit quite different FWHM values and extinction intensities as compared to the dimer. Indeed, it can be seen in Fig. 1(g) where we compare the scattering at $\theta \approx 51°$ for the dimer and $\theta \approx 55°$ for the monomer that the dimer coupling results in narrower peaks (smaller FWHM magnitudes) especially around modes p1 and p2 with much enhanced scattering. These results show the interest of dimers over monomers in terms of higher amplitudes of the localized fields due to the more strongly excited modes, with a perspective of enhanced OMC. Such finding about improved FWHM values and higher scattering intensities with dimers is similar to what have been reported elsewhere [28]. To get a deeper insight about the origin and behavior of the observed modes, we study in Fig. 2 the dimer scattering evolution versus wavelength and geometrical parameters. We first analyze the effect of the ridges width D_{Au}, where the remaining parameters are kept constant and equal to the values chosen earlier (Fig. 1).

Throughout this paper, we focus on scattering spectrum alone, given that this quantity is nearly an order of magnitude higher than absorption. In Fig. 2(a) is shown the scattering cross section

Optics EXPRESS

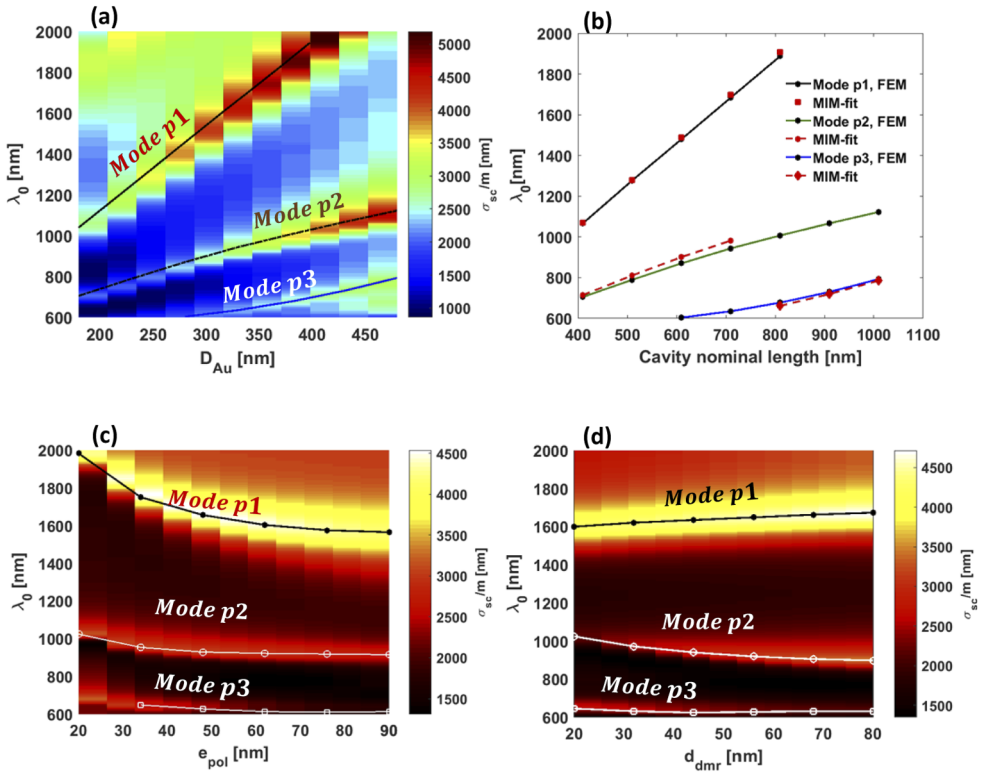

Fig. 2. (a) Scattering cross section per unit length of the geometry design in Fig. 1(b) versus wavelength and ridges width D_{Au}. (b) Plot of the resonance wavelengths of modes p1, p2 and p3 as a function of the MIM-like effective cavity formed under the dimer (Fig. 1(b)) with the nominal length $L_{nom} = (2D_{Au} + d_{dmr})$. In the plot, FEM-based numerical results are fitted with MIM cavity-based model. (c), (d) Same as in (a) but versus wavelength and polymer thickness e_{pol} or dimer inter-distance d_{dmr}.

of the dimer per unit length versus D_{Au}, and as a guide for the eye, we have overlaid the plot of resonance wavelengths (corresponding to scattering maxima positions) associated with modes p1 (solid black line), p2 (black dashed-dotted line) and p3 (solid blue line). The resonance wavelength λ_1 of mode p1 linearly increases with D_{Au}, whilst the linear trend is obtained only at smaller widths for mode p2 and at larger widths for mode p3. The reason, as detailed below, is the fact that mode p1 is highly localized in the polymer below the ridges while modes p2 and p3 can display a significant localization in the vertical area between the two ridges (vertical MIM-components). The noted behavior of the modes can be captured using a MIM-like effective cavity-based model [58], corresponding roughly to the space under the dimer where the modes are localized. Such cavity has then a nominal length $L_{nom} \sim 2D_{Au} + d_{dmr}$ and a thickness of e_{pol}. Following this approach, resonance wavelengths corresponding to plasmonic standing waves that form due to reflections-off the dimer edges are obtained by:

$$\lambda_{r0} = \frac{2n_{eff}L_{nom}}{m} \tag{1}$$

where, $n_{eff} = k_{spp}/k_0$ is the effective refractive index of the propagating MIM-like plasmon (k_{spp} being its wave vector) and $m = 1, 2 \ldots$ is an integer. This equation arises from a resonance condition due to a round-trip in the cavity by the plasmon, that is, $2k_{spp}L_{nom} + 2\varphi_{ref} = \pi m$, where

Optics EXPRESS

φ_{ref} is the phase-shift due to reflection-off dimer edges. The account for φ_{ref} is realized through the approximation $\varphi_{ref} \approx k_{spp}\delta L$ [58] so that the actual cavity length becomes, $L_{eff} \approx L_{nom} + \delta L$, where δL is an additional apparent length translating modes extension further the edges; its value is adjusted in order to obtain a good fit to the numerical data and depends on each mode (see below). The following values for the apparent additional cavity length, i.e. $\delta L \sim 195$ nm for mode p1, $\delta L \sim 211$ *nm* for mode p2 and $\delta L \sim 45$ *nm* for mode p3, were necessary to reach the observed fit. Note that these values mean that the plasmonic modes extend further the edges by half of such values on each (edge) side.

Let us point out that in the cavity-MIM model the resonance wavelength changes linearly with L_{eff}, meaning only linear trends of the plasmonic modes p1, p2 and p3 with the cavity length can be captured with the model. Such linear trends correspond to strongly confined MIM-components of the modes under the dimer, dominating or being comparable in terms of field intensity with the vertical components in between the ridges, whilst for the non-linear parts of the trends, the vertical MIM-components dominate as will be shown in the following. Based on the E_s field localization shown in Figs. 1(d)–1(f), we deduce that for mode p1, $m \approx 2$ while $m \approx 4$ and $m \approx 5$ for modes p2 and p3, respectively. Comparison of the numerical and MIM-cavity based fit plots are summarised in Fig. 2(b). One notes the quasi-perfect accord seen for mode p1, whereas for mode p2 a good fit is obtained at smaller widths and for mode p3 the good agreement is seen at larger D_{Au} values. This matches the noted linear trends of the modes in Fig. 2(a). As just mentioned, this also reflects that for mode p2 the horizontal MIM-component is dominant (or comparable to the vertical-component) for small widths of the cavity, while for mode p3 such component is dominant for larger D_{Au} values. Indeed, in Supplement 1 (Figs. S2(a)), we show that mode p2 field localization for $L_{nom} = 510$ *nm* is the same, both under and between the ridges. This observed field localization property remains valid as long as $L_{nom} \lesssim 710$ *nm*, where the resonance wavelength of mode p2 changes linearly with L_{nom} and fits well the numerical data. Similarly, mode p3 field localization rate shown in Supplement 1 (Fig. S2(b)) for $L_{nom} = 910$ *nm* indicates about two times more intense field under the dimer comparing with vertical component, meaning the former dominates the latter and hence the linear trend. Such behavior is valid as long as $L_{nom} \gtrsim 810$ *nm*. Effects of e_{pol} and d_{dmr} are shown in Figs. 2(c)–2(d) where scattering is plotted against wavelength and these parameters, respectively. We overlay modes 1, 2 and 3 resonance wavelengths changes versus the parameters with the scattering map to better show their behaviors. Based on the fact that a guided MIM-type plasmon effective refractive index n_{eff} varies as $\propto 1/d$, where d is the MIM-guide width [59], one can explain mode p1 evolution versus e_{pol} (Fig. 2(c)). The latter is a MIM-like LSP confined in the polymer with thickness e_{pol}, of resonance wavelength $\lambda_1 \propto n_{eff}$ leading roughly to $\lambda_1 \propto 1/e_{pol}$. For mode p2, for small e_{pol} ($\leq$50 *nm*), the mode is strongly confined in the polymer, based on E_s-field map shown in Supplement 1, Figs. S2(c)-S2(d). Thus, this mode component, i.e. under the ridges, is sensitive to e_{pol}, and we approximately get a decrease of λ_2 such as $\lambda_2 \propto 1/e_{pol}$ while for larger e_{pol} the vertical component becomes more dominant (see Supplement 1, Fig. S2(d)) and sensitivity versus e_{pol} is lost. For the same reason, mode p3 is also sensitive to smaller e_{pol} values and nearly not as the latter increases.

As concerns d_{dmr} effect (Fig. 2(d)), the mode p1 of wavelength λ_1 shifts linearly with d_{dmr} which simply relates that increasing d_{dmr} results in increasing $L_{eff} \sim (2D_{Au} + d_{dmr} + \delta L)$, leading to nearly $\lambda_1 \propto L_{eff}$. For mode p2, highly confined between the ridges, λ_2 behaves as $\lambda_2 \propto 1/d_{dmr}$. Mode p3, on the other side, is weakly sensitive to d_{dmr}, except for very smaller values of this parameter ($\sim\leq$55 *nm*) where the vertical component is dominant over the one under the dimer (as can be seen in Supplement 1, Fig. S2(e)); then we get a behavior near to $\lambda_3 \propto 1/d_{dmr}$.

Optics EXPRESS

3. Dimer mechanical eigenmodes and OMC coefficients

In this section, we study numerically using finite element method the dimer-FCN mechanical eigenmodes. First, we consider a periodic ridge structure and use Bloch periodic boundary conditions (along x-axis) to determine the dispersion curves. In order to get the modes of an isolated dimer, we set the system period to a sufficiently large value such as $a \approx 5\ \mu m$. Unlike for optical modelling, the analysis of the mechanical eigenmodes requires to incorporate the SiO_2 substrate as sketched in Fig. 3(a). Note that we have used SiO_2-based PMLs at the bottom of the latter to mimic a semi-infinite SiO_2-substrate. Let us also mention that the polymer material is an isotropic medium whose elastic properties are represented by Young modulus $E = 3.6\ GPa$, Poisson ratio $\nu = 0.34$ and density $\rho = 1420\ kg/m^3$. Similarly, SiO_2 is also considered as an isotropic medium with $E = 72.2\ \ GPa$, $\nu = 0.168$ and $\rho = 2200\ kg/m^3$. On the other side, gold is an anisotropic material with face centered cubic crystal structure whose elastic constants C_{11}, C_{12} and C_{44} were taken from Ref. [9]. Simulated dispersion curves for $D_{Au} = 320\ nm$, $h_{Au} = 300\ nm$, $e_{pol} = 50\ nm$ and $d_{dmr} = 50\ nm$ are shown in Fig. 3(b). We focus on Brillouin zone edge states situated under SiO_2-sound line (localized phonons) and some other modes above the latter which nevertheless correspond to modes localized in the vicinity of the surface. We refer to these modes as A1, A2, B1, B2, and A3 up to A5 (Fig. 3(b)). In Fig. 3(c), we show the maps of the displacement field norm associated with these modes. We observe that modes A1 situated at ~0.215 GHz and A2 at ~0.246 GHz are in-phase and out-of-phase flexural modes respectively, originating from the split of a monomer flexural mode caused by the dimer mechanical coupling. Mode B1 found at ~0.29 GHz corresponds to a Sezawa type surface mode with symmetric bending vibration of the polymer/gold films, while in mode B2 (which is also a Sezawa surface mode at ~0.34 GHz) the antisymmetric bending motion of such films cause the dimer to have an in-phase flexural vibration, according to the shape of such modes shown in Supplement 1, Figs. S3(a)-S3(b). On the other hand, mode A3 found at ~0.4756 GHz is the in-phase compressional dimer mode slightly coupled with a Sezawa-like mode of the polymer/gold films, whereas mode A5 at ~0.557 GHz is the out-of-phase compressional mode of the dimer. Both modes originate from the split of the monomer ridge compressional mode. Finally, mode A4 situated at ~0.514 GHz is a complex high order flexural mode with torsional components of the dimer, also coupled to the films. This mode shape can be seen in Supplement 1, Fig. S3(d). The optomechanic coupling (OMC) of the acoustic modes with the plasmons studied above can be quantitatively determined from the computation of coupling coefficients, g_{OM}. This parameter has frequently been employed to evaluate the coupling strength between an eigen- mechanical and an optical mode in a simultaneous acoustic and photonic cavity [13,14]. Such coefficients originate from the volume photo-elastic effect and surface moving interface effect [13], and their expressions can be obtained using a first-order perturbation theory [13,60] based on the knowledge of the acoustic and optical fields in the dimer, such as:

$$g_{PE} = -\frac{\omega}{2}\frac{\left\langle \vec{E}\middle|\delta\varepsilon\middle|\vec{E}\right\rangle}{\iiint_V \vec{E}.\vec{D}dV}\sqrt{\frac{\hbar}{2M_{eff}\Omega}} \tag{2}$$

$$g_{MI} = -\frac{\omega}{2}\frac{\oint_S (\vec{U}.\vec{n})(\Delta\varepsilon\vec{E}_{\parallel}^2 - \Delta\varepsilon^{-1}\vec{D}_{\perp}^2)d\vec{S}}{\iiint_V \vec{E}.\vec{D}dV}\sqrt{\frac{\hbar}{2M_{eff}\Omega}} \tag{3}$$

where, M_{eff} is the effective motional mass which is defined in relation to the (normalized) mechanical displacement field $\vec{U}$ as $M_{eff} = \iiint_V \rho\vec{U}^2 dV$, where ρ is the mass density, $\vec{D}$ is the

Optics EXPRESS

electric displacement field, $\vec{E}$ is the electric field, and $\vec{n}$ is the outside normal to the ridges boundary, while Ω and ω are respectively the acoustic and the optical frequencies. It should be mentioned that in the calculation of the effective mass M_{eff}, the ridges are in principle considered as infinitely long along y-axis (see Fig. 1(a)), meaning that their length parallel to such dimension is such as $L_y \gg D_{Au},\ h_{Au}$. Specifically, L_y intervenes directly in the calculation of M_{eff} which is defined in two dimensional calculations as $M_{eff} = \iint_S \rho \vec{U}^2 dS \times L_y$, where S is the section of the system. As a result, both g_{PE} and g_{MI} magnitudes are $\propto 1/\sqrt{L_y}$, that is to say, bigger L_y values yield lower values of g_{PE} and g_{MI}. In Figs. 3(d) and (e), we have chosen to set the ridges length as $L_y = 3.5\ \mu m > 10 D_{Au} \gg D_{Au} = 320\ nm\ \sim\ h_{Au} = 300\ nm$. Furthermore, $\Delta\varepsilon = \varepsilon_1 - \varepsilon_2$, with ε_1 and ε_2 being the dielectric permittivities of the materials on both sides of an interface, and $\delta\varepsilon$ is the amount by which each ridge (of the dimer) dielectric permittivity is shifted due to (volume) acoustic strain.

Here, we employ the approach detailed in [61,62] to determine such volume effect shift in dielectric permittivity, $\delta\varepsilon$, in metals. The computed $g_{OM} = g_{PE} + g_{MI}$ versus dimer acoustic eigen-modes frequency are shown in Figs. 3(d)–3(e), where we have chosen to study coupling with MIM-LSP modes p1 ($\sim$ 1638 nm) and p2 ($\sim$ 926 nm) given that these mode are more strongly excited (Fig. 1(g)) and better confined (Figs. 1(d)–1(e)). Let us indicate that such localized plasmons are excited as earlier in Fig. 1(c) i.e., by setting up a scattering problem where an air domain surrounded by PMLs is added on top of the geometry in Fig. 3(a), and that incoming light is incident with an angle of 51°. As concerns mode p1 (Fig. 3(d)), we note that mode B1 at $\sim 0.29\ GHz$ yields the strongest OMC such as $g_{OM}(B1)/2\pi \approx 0.0782\ MHz$, followed by the in-phase compression mode A3 at $\sim 0.4756\ GHz$ with $g_{OM}(A3)/2\pi \approx 0.0712\ MHz$, and by out-of-phase flexural mode A2 (at $\sim 0.245\ GHz$) which also indicates a significant coupling as $g_{OM}(A2)/2\pi \approx 0.0307\ MHz$. The remaining modes A4 and B2, show a weaker coupling such that $g_{OM}(A4) > g_{OM}(B2)$, while modes A1 and A5 with $g_{OM}(A5) \approx g_{OM}(A1)$ are nearly inactive optomechanically. The strong coupling of modes B1, A3 and mode A2 (with a lesser magnitude) with the plasmon p1, can be explained by the fact that such modes according to their shape (see Fig. 3(c) and Fig. S3(c)) compress/stretch the effective MIM-cavity volume under the dimer in their compression movement (along $z-$axis), hence the high g_{OM}-values. The rest of the modes overlap less (modes A4 and B2) or much less ($A1$ and A5) with the plasmon confined in the cavity, which results in lower or much lower g_{OM}-values. In Fig. 3(e), we present the optomechanical couplings coefficients of the MIM-LSP mode p2, where we note different g_{OM}-values depending on each mode. Specifically, modes B1 and A3 which show the highest OMC such as $g_{OM}(B1)/2\pi \approx 0.0387\ MHz$ and $g_{OM}(A3)/2\pi \approx 0.0284\ MHz$, indicate a sensible fall of the optomechanical coupling rate comparing with mode p1. Out-of-phase flexural mode A2 also manifests a drop in OMC as the coupling coefficient falls down to $g_{OM}(A2) \setminus (2\pi) \approx 0.0121\ MHz$. Such trend could be related to the fact that the plasmon p2 is significantly less strongly excited (see Fig. 1(g)) and confined as compared to mode p1, leading to a weaker overlap and thus to a weaker coupling magnitude with the modes B1, A3 and A2. On the other side, except for modes A1 whose optomechanical coefficient gets further lowered down rendering it quite inactive, the rest of the modes A1, B2, A4 and A5 show a simi lar tendency comparing with mode p1 as their coefficients do not change much, which might relate to their weak overlap with mode p2 in an equivalent fashion as with mode p1. It is worth mentioning that the very low OMC of mode A5 can be linked to the fact that in this mode, as one of the ridges compresses the MIM-cavity, the other one stretches it out at the same instant, resulting in almost a null effect. We would like to point out that the coefficient g_{PE} representing the volume effect is found to be quite small comparing with g_{MI} (surface effect) for all modes, which probably relates to the fact that the plasmons modes (p1 and p2) show a strong localization near metal interfaces and a quite weaker confinement within the metal volume.

Optics EXPRESS

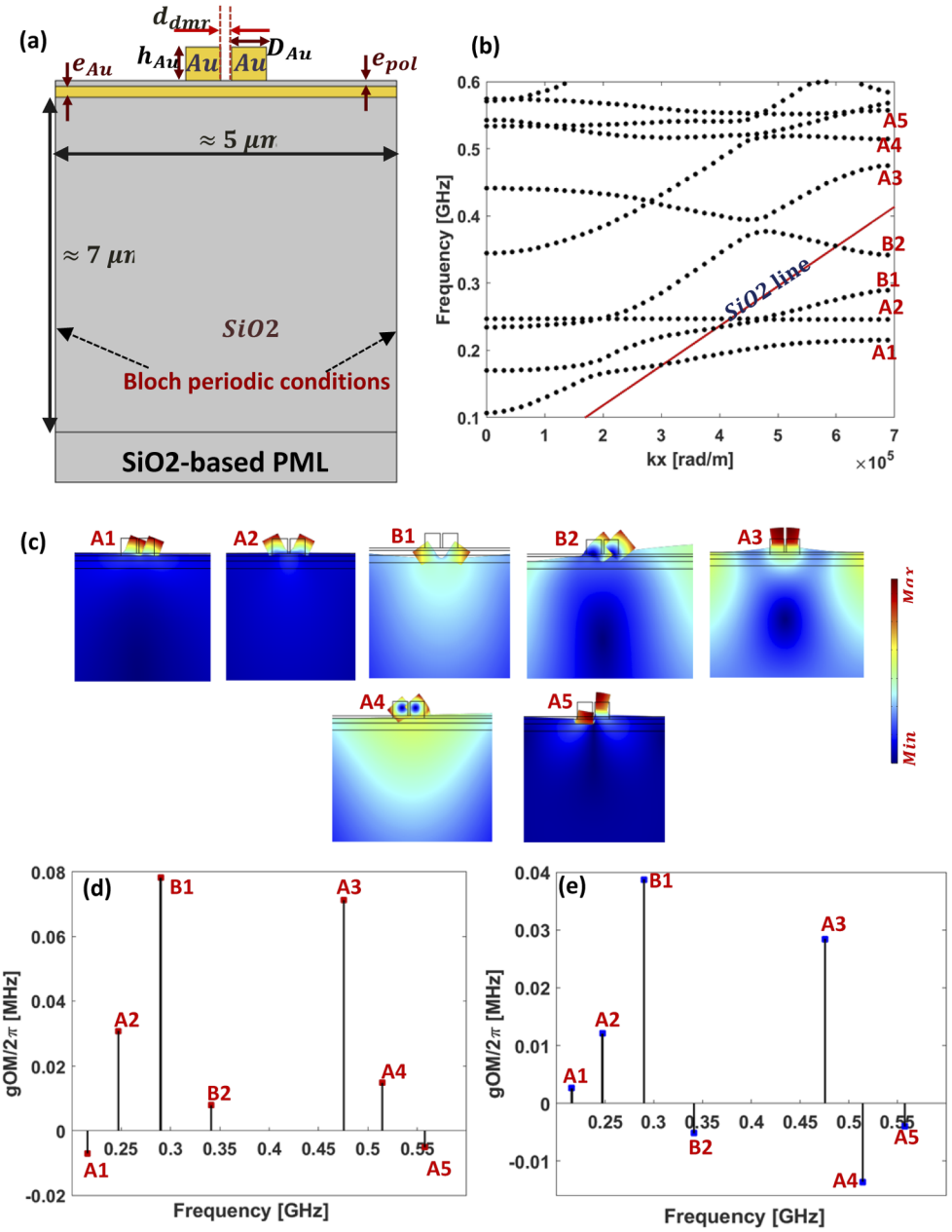

Fig. 3. (a) Sketch of the dimer-FCN geometry employed to study the system acoustic modes. The structure is put atop a SiO2 substrate, and Bloch periodic conditions are set along $x-$axis so to compute the dispersion curves. The period $a \approx 5\ \mu m$ is chosen large enough in order to isolate the dimer. (b) Corresponding simulated dispersion curves for the following geometrical parameters: $D_{Au} = 320\ nm$, $h_{Au} = 300\ nm$, $e_{pol} = 50\ nm$ and $d_{dmr} = 50\ nm$. (c) Displacement field norm map near and around the dimer at the frequencies of the Brillouin Zone edge modes referred to as A1, A2, B1, B2 and A3-A5 in the dispersion plot of (b). (d), (e) Computed optomechanical coupling (OMC) coefficients of the acoustic modes depicted in (c) with the MIM-LSP modes p1 (~ 1638 *nm*) and p2 (~ 926 *nm*) shown in Fig. 1(c), respectively. Note the different scale of such plots.

Optics EXPRESS

4. Surface acoustic waves monitoring of OMC in the dimer FCN-based design

4.1. Transmission properties of SAW

We now investigate the coupling of the LSP-plasmons (modes p1 and p2 of Figs. 1(d)–1(e)) with the eigen-mechanical modes of the dimer excited by means of SAWs. Let us first study the transmission properties of SAW through the system in the frame of the scheme depicted in Fig. 4(a). Perfect matched layers are set to surround the whole simulation domain preventing any unwanted reflections. Geometrical parameters of the dimer and those characterizing the FCN structure are chosen as earlier in Fig. 3(b). For obvious symmetry reasons of invariance along $y-$axis, we perform 2D simulations within a section (in a ozx-cut plane) of the geometry in Fig. 4(a). An excitation line force is applied atop the system vertically along $z-$axis as shown in Fig. 4(a). The transmission coefficient is obtained by making an average of the displacement field magnitude $\sqrt{|u|^2+|w|^2}$ registered at the detection point (Fig. 4(a)) and normalized with respect to the structure in absence of the dimer. In Fig. 4(b), we show an example of SAW effective excitation and propagation near the surface of the system, where we have depicted $|w|/\max\left(\sqrt{|u|^2+|w|^2}\right)$ map. Here, the displacement field max is evaluated within the whole structure. The transmission spectrum is computed in the frequency range $[0.12\ GHz - 0.62\ GHz]$ which covers all the dimer-FCN eigen-mechanical modes studied above. Figure 4(c) shows the transmission coefficient for the system sketched in Fig. 4(a), and as a matter of comparison, we have also plotted the transmission of the same structure but for a gold ridge monomer of same dimensions.

In case of the monomer (black curve), one notes the excitation of three modes in the frequency range of interest, that is, $f_{M1} \approx 0.234\ GHz$ (mode M1), $f_{M2} \approx 0.5218\ GHz$ (mode M2) and $f_{M3} \approx 0.615\ GHz$ (mode M3). These modes correspond, according to the displacement field maps of Fig. 4(e), to a first flexural, a compressional and a higher order flexural mode, respectively. When a dimer is set atop the structure instead (red curve), we observe due to dimer mechanical coupling a split of the modes M1 and M2 while the split of mode M3 shifts out of the frequency domain. Mode M1 gives rise to in-phase and out-of-phase flexural modes at $f_{D1} \approx 0.222\ GHz$ (mode D1) and $f_{D2} \approx 0.24724\ GHz$ (mode D2), respectively, while mode M2 splits respectively into in- and out of-phase compressional modes at $f_{D3} \approx 0.4748\ GHz$ (mode D3) and $f_{D4} \approx 0.548\ GHz$ (mode D4). This is seen in Fig. 4(f) where displacement maps around the dimer at these modes frequencies are plotted. On the other hand, mode D5 at ~0.6056 GHz, originating from the split of mode M3, has some common features with the in-phase flexural high order mode A4 seen in Fig. 3(c), even if slightly different, as the dimer is isolated. Indeed, mode A4 being coupled with the polymer/gold films is somewhat related to the system (Fig. 3(c)) periodicity. Modes B1, B2 which are not excited with SAW, originate probably essentially from periodic weak coupling in the design of Fig. 3(a), hence their missing in the transmission spectrum.

It is worthwhile mentioning that the dimer modes excited with SAW match well with those obtained in the dispersion curves of Fig. 3(b). There are only very small shifts in frequencies. For instance, the in-phase compressional mode D3 frequency in the fully isolated structure (Fig. 4(a)) is found as ≈0.4748 GHz instead of ≈0.4756 GHz for mode A3 in the periodic geometry of Fig. 3(a). For the other modes excited by SAW, we have the following correspondence with the modes of Fig. 3(b): (in-phase flexural) D1 at $f_{D1} \approx 0.222\ GHz \leftrightarrow$ A1 at $f_{A1} \approx 0.215\ GHz$, (out-of-phase flexural) D2 at $f_{D2} \approx 0.24724\ GHz \leftrightarrow$ A2 at $f_{A2} \approx 0.246\ GHz$, and out-of-phase compressional D4 found here at $f_{D4} \approx 0.548\ GHz \leftrightarrow$ A5 at $f_{A5} \approx 0.557\ GHz$.

Furthermore, we have studied in the Supplement 1 the dimer/monomer-FCN mechanical eigenmodes using a different approach instead of SAW (Fig. 4(a)) consisting in exciting the dimer/monomer locally and probing the excited modes also locally. This complementary approach

Optics EXPRESS

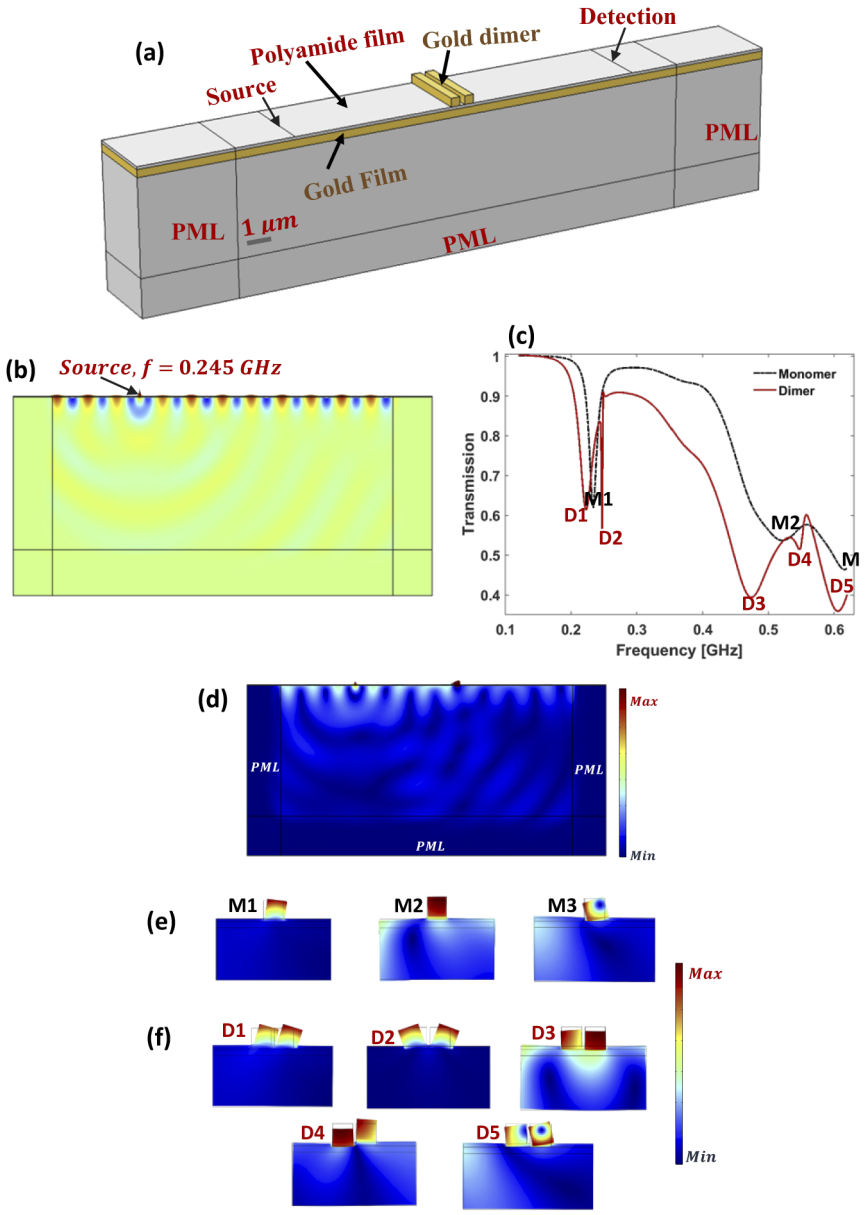

Fig. 4. (a) Scheme of the dimer-FCN geometry design for the study of SAW transmission. Similar to Fig. 3(a), the structure is deposited on SiO_2 substrate and PMLs are surrounding it to get rid of undesired reflections. (b) Plot at $f = 0.245\ GHz$ of absolute magnitude of the displacement field component w, normalized to the displacement field norm maximum measured in the whole system, in absence of the dimer. (c) Transmission coefficient through a dimer (red curve) or a monomer (black curve). The transmitted amplitude is normalized to that of a flat surface without ridges. (d) Displacement field norm map in the geometry at the frequency, $f_{D1} \approx 0.222\ GHz$, of the mode referred to as D1 in (c). (e) Zoom in of displacement field norm map around the monomer at the frequencies, $f_{M1} \approx 0.234\ GHz$, $f_{M2} \approx 0.5218\ GHz$ and $f_{M3} \approx 0.615\ GHz$ of the modes referred to as M1, M2 and M3 in (c). (f) Same as in (e) but for modes referred to as D1 up to D5 in (c), whose frequencies are, respectively, $f_{D1} \approx 0.222\ GHz$, $f_{D2} \approx 0.24724\ GHz$, $f_{D3} \approx 0.4748\ GHz$, $f_{D4} \approx 0.548\ GHz$ and $f_{D5} \approx 0.6056\ GHz$.

Optics EXPRESS

gives also an overall good agreement within a few percent frequency shifts. It is interesting to note the higher quality factors of the dimer modes D1 and D2 (Fig. 4(c)) comparing to the other modes due to their higher localization degree in the dimer.

Based on the findings in Figs. 3–4, we will focus on OMC of the dimer acoustic modes showing the highest g_{OM} coefficients and which are fairly well excited by SAW, that is, the in-phase compressional mode D3 and the out-of-phase flexural mode D2. In order to study OMC using SAW, we employ the geometry in Fig. 4(a) on top of which (near the dimer) we add an air domain for optical calculations. PMLs are set to surround the latter to avoid reflections. We search for optical quasi normal eigenmodes of interest p1 and p2 by virtue of complex eigen- frequency simulations. A sketch of the geometry is shown in Fig. 5(a). We follow the method of moving mesh detailed elsewhere [38,46] to calculate the modulation of the dimer plasmon mode by the considered mechanical mode. Specifically, at an instant of time of the deformed geometry (quasi-static approximation [38]) due to SAW-excited dimer mechanical mode we calculate the new shifted resonance plasmon mode frequency using optical quasi-normal eigenfrequency calculations. For the purpose of numerical simulation, the elastic deformation should not be too small, neither large as compared to the mesh size.

Therefore, we opt for a mesh deformation such that the maximum elastic displacement allowed inside/near the ridges is about $u_{max} \approx 1.55\ nm$, meaning a small deformation rate equal to ~ 0.48 % the width of the ridge. The applied max displacement u_{max} is adjusted through the tuning of the excitation force magnitude that gives rise to the SAW at the inlet of the system. In the followings, we set the same u_{max} in the simulations of all the considered phononic modes by adapting the strength of the force that creates the SAW. However, it should be noted that in an actual experiment with a given strength of the applied voltage to the intertigitated transducers, the acoustic deformation of the ridge structure will be different from one phononic mode to another. This means that the corresponding plasmonic modulation needs to be evaluated accordingly by applying a rule of three. In other words, the efficiency of plasmonic modulation will depend both on the intrinsic OMC and on the ability of the SAW to excite the considered phononic mode with a large amplitude. This remark will be applied to the modes D2 and D3 and discussed below.

In Fig. 5(b), we have plotted for the in-phase compressional mode D3 the shift in the plasmon eigen-wavelength, such as $\delta\lambda_1 = \lambda_1 - \lambda_{10}$, where λ_{10} is the original wavelength while λ_1 is the modulated wavelength, versus the temporal phase $\phi = (2\pi) \times f_a \times t$ of the acoustic wave, with $\phi \in [0 - 2\pi]$. Here, f_a is the frequency of the acoustic mode while t is the time; the considered MIM-LSP is mode p1 found at $\sim 1638\ nm$ in Fig. 1(c). Similarly, in Fig. 5(c) we analyze the modulation of the plasmon mode p2 at $\sim 926\ nm$ (Fig. 1(c)) by the same acoustic mode D3. We show in Supplement 1 (Figs. S5(a)-S5(c)) the E-field norm maps of plasmonic modes p1, p2 and that of a monomer giving rise to mode p1 by using the complex eigen-frequency method. These maps are very similar to those obtained by the scattering calculations (Fig. 1(c)). We note that the mode D3 of the dimer strongly modulates the plasmon mode p1 (Fig. 5(b)) as the latter resonance wavelength undergoes a periodic oscillation with a maximal amplitude of $\delta\lambda_1 \approx 6.4\ nm$ around $\lambda_{10} \approx 1613\ nm$. Plasmon mode p2 is also periodically modulated with lesser magnitude (Fig. 5(c)) since the maximum modulation amplitude is of $\delta\lambda_2 \sim 2.7\ nm$ where $\lambda_{20} \approx 900\ nm$. The strong OMC noted here is due to the important deformation induced by the compressional mode within the MIM-cavity under the dimer whose volume compresses/stretches as the mode oscillates, hence the plasmon modulation.

This is particularly true for plasmon mode p1 which is more strongly localized (see Supplement 1, Figs. S5(a)-S5(b)) in the cavity as compared to plasmon mode p2 less intensely confined underneath the dimer.

Also, this is consistent with the computed g_{OM} in Figs. 3(d)–3(e), showing a stronger optomechanical coupling magnitude with mode p1 than with mode p2. Specifically, one notes that the ratio expressing the fall of the OMC strength of mode A3 with modes p1 and p2 from Fig. 3(d)

Optics EXPRESS

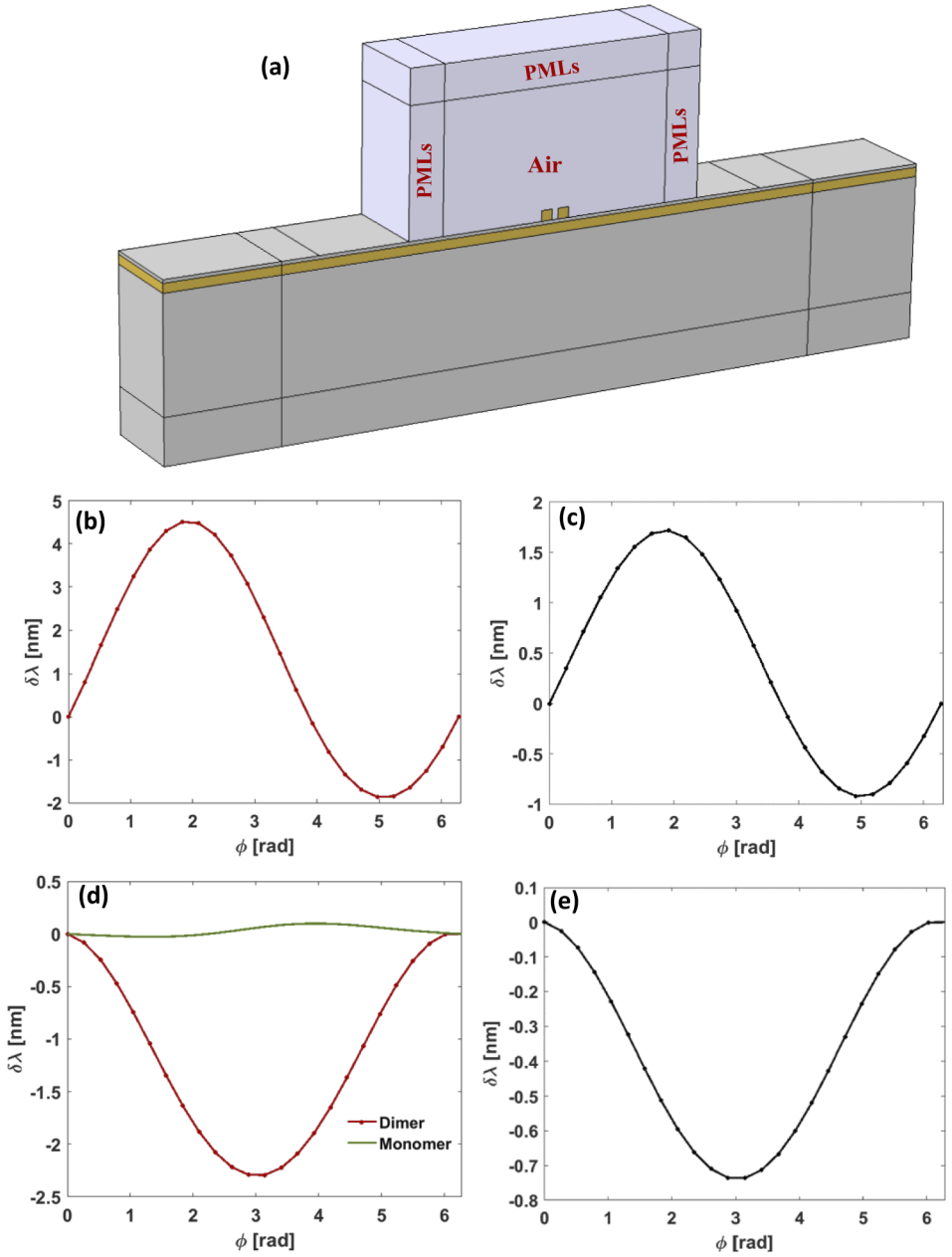

Fig. 5. (a) Sketch of the SAW-based geometry similar to the one in Fig. 4(a) but on top of which an air domain is added over the dimer for optical eigen-frequency simulations. PMLs are placed all around the air domain to eliminate reflections. (b), (c) Modulation of the resonances wavelengths $\delta\lambda = \lambda - \lambda_{i0}$ (with, $i = 1,\ 2$) of plasmonic modes p1 and p2 by in-phase compressional mode D3 versus the temporal phase. The wavelengths λ_{i0} correspond to the original unmodulated plasmonic resonances found at $\lambda_{10} \approx 1613\ nm$ for mode p1 and at $\lambda_{20} \approx 900\ nm$ for mode p2 by quasi-normal optical modes search. (d), (e), Same as in (b) and (c) but in case where the modulating mechanical mode is the in-phase flexural mode D2. As for comparison of OMC rates between a dimer and monomer, in (d) we also plot in dark green curve, the modulation of the equivalent of plasmon p1 in case of a monomer atop the polymer by the flexural mode of a monomer (mode M1).

Optics EXPRESS

($A3 \leftrightarrow p1$) to Fig. 3(e) ($A3 \leftrightarrow p2$) is such as $g_{OM}(A3 \leftrightarrow p1)/g_{OM}(A3 \leftrightarrow p2) \approx 0.0712/0.0284 \approx 2.50$. In Figs. 5(b)–5(c) such ratio takes the form $\delta\lambda_1(D3 \leftrightarrow p1)/\delta\lambda_2(D3 \leftrightarrow p2) \approx 6.4/2.7 = 2.37$, which compares rather well with the former taking into account the differences between the systems in Figs. 3(a) and 5(a). Indeed, the dimer in the periodic structure of Fig. 3(a) is not fully isolated and its eigen-modes in terms of their shape in particular are rigorously determined whereas in Fig. 5(a), the dimer modes are more or less efficiently excited with a more or less important FWHM by the SAW, which might explain the noted small discrepancy. As concerns the interaction of mode D2 with plasmons p1 and p2, the results are depicted respectively in Fig. 5(d) and Fig. 5(e). Both modes are periodically modulated by the phonon, with the associated maximum modulation amplitudes, $\delta\lambda_1 \approx 2.3$ *nm* for mode p1 and $\delta\lambda_2 \approx 0.74$ *nm* for mode p2. The latter is weaker than the values obtained above while the former is quite significant. As can be seen in Supplement 1 (Fig. S3(c)), where mechanical displacement field norm is depicted in the dimer and underneath within the effective MIM- cavity at the frequency of mode D2 ~0.246 *GHz*. One notes the cavity volume deformation (i.e., a combination of compression/stretching) in such mode, supporting why $\delta\lambda_1$ reaches the observed value. The observed coupling strengths of mode D2 with modes p1 and p2 shown in Figs. 5(d)–5(e) agree well with the simulated g_{OM} of such mode in Figs. 3(d)–3(e).

As a matter of fact, in the latters we have $g_{OM}(A2 \leftrightarrow p1)/g_{OM}(A2 \leftrightarrow p2) \approx 0.0307/0.0121 \approx 2.54$, while in Figs. 5(d)–5(e) the OMC strength is given by $\delta\lambda_1(D2 \leftrightarrow p1)/\delta\lambda_2(D2 \leftrightarrow p2) \approx 2.3/0.7 = 3.28$, showing that both values are quite close. As mentioned above, the small discrepancy between the two can be probably attributed to the differences between the systems sketched in Figs. 3(a) and 5(a).

Actually, one might expect a better OMC rate between mode D2 and plasmon mode p2 as the latter has a MIM-like component confined vertically between ridges, which should be compressed/stretched by such mode. Nonetheless, in Hooshmand and El-Sayed work on nanocubic silver dimer interaction, the strong coupling regime where plasmons modes splitting occurs, is attained for inter-dimer distances of $d_{dmr} \sim 2\ nm - 5\ nm$ [63]. That means that our coupled dimer for which, $d_{dmr} = 50\ nm$, is rather in the moderate to weak coupling regime which results in a weaker vertical MIM component of plasmon mode p2, and hence a weaker overlap between such plasmon and mode D2, translated by a lower plasmon modulation. Another possibility to explain the value of $\delta\lambda_2 \approx 0.74$ *nm* resides in the fact that in mode D2 the gap between the ridges is rather compressed at their bottom, near the polymer, and stretched asymmetrically at the upper side and vice-versa during an oscillation (see mode shape in Fig. S3(c)). As a result, a compensation takes place in the plasmon resonance wavelength shift, yielding an overall weaker modulation.

The equivalent of plasmon mode p1 for a monomer atop with a strong confinement under the ridge is found by quasi-normal eigen-frequency simulations at $\lambda_0 \sim 1800\ nm$; the map of its electric field norm is shown in Supplement 1, Fig. S5(c). The corresponding modulation $\delta\lambda = f(\phi)$ by the flexural mode M1 giving rise to D2 mode in case of a dimer is also plotted in dark green curve in Fig. 5(d). It can be seen that the flexural mode of monomer seemingly inactive optomechanically becomes clearly active in case of a dimer in the out-of- phase flexural motion of mode D2, the reason being related to the cavity volume deformation in such mode as mentioned earlier. Note that the dimer mode D1 having the exact same symmetry as for the monomer flexural mode M1 remains inactive.

Besides the intrinsic OMC, the efficiency of the plasmonic modulation depends also on how the generated SAW will be able to strongly excite the localized phonons of the dimer ridges. Indeed, for a given strength of the force exciting the SAW, one can compare the maximum amount of deformation and compare it to the value fixed to 1.55 nm in the simulation of the intrinsic OMC. Indeed, the maximum plasmon oscillation amplitude $\delta\lambda$ (nm) is linearly scalable with u_{max} as long as we stay in the linear regime, supported by the sinusoidal shapes of the

Optics EXPRESS

modulation wavelengths shown in Fig. 5. As an illustration, let us assume an applied force of 1.2 N to generate SAW. Then, we observe a maximum displacement field of 1.55 nm and 44.3 pm respectively for the flexural D2 mode and the compressional D3 mode. Clearly, the SAW excites much more strongly the flexural mode D2 than the compressional mode D3. As a consequence, mode D2 will become much efficient optomechanically with a max modulation of $\delta\lambda \approx 2.3$ nm according to Fig. 5(d); while simulations show that with a maximum displacement of 44.3 pm set in mode D3, the obtained plasmon modulation is of $\delta\lambda \approx 0.1674$ nm i.e., $\sim$ 14 fold smaller.

It is interesting to show the modulation of the plasmons through the shift of the dimer scattering cross section caused by the localized mechanical mode excited by the SAW. As a matter of fact, the scattered field is experimentally detected. Hence, we set out to simulate scattering cross section σ_{sca}/m shift by the compressional mode D3 around plasmon modes p1 and p2 at different temporal phases of the acoustic mode. The results are shown in Figs. 6(a) and Fig. 6(b), where we have plotted σ_{sca}/m versus wavelength at the phases, $\phi = 2$ $[rad]$, and 5 $[rad]$ for plasmon modes p1 and p2, respectively. These phase values correspond to the positions of maximum plasmon wavelength modulation, according to Figs. 5(b)–5(c). Let us mention that such scattering simulations are performed using the SAW-geometry design depicted in Fig. 5(a).

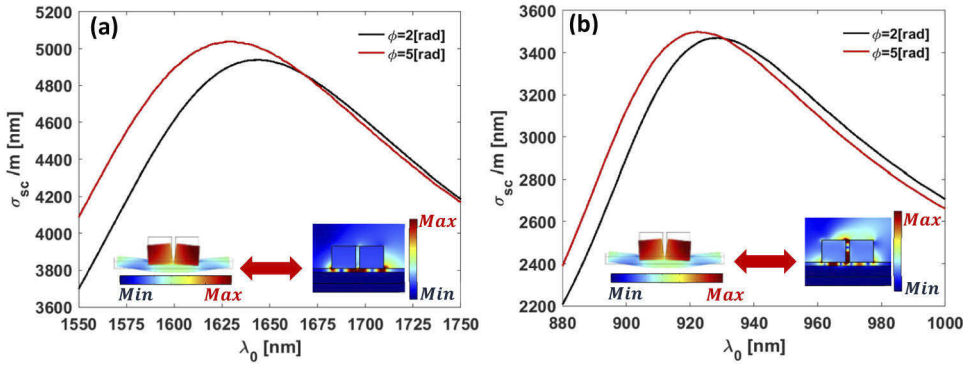

Fig. 6. (a) Scattering cross section plotted versus wavelength of the dimer in the geometry of Fig. 5(a). The frequency range is chosen around the plasmon mode p1 at $\sim$ 1638 nm (Fig. 1(c)). Incidence angle of the incoming field is set as $\theta \approx 51°$ (similar to Figs. 1(d)–1(e)). (b) Same as in (a) but around the wavelength range of plasmon mode p2 at $\sim$ 926 nm (Fig. 1(c)). Insets show dimer compression mode D3 interacting opto-mechanically with plasmon mode p1 in (a) and with plasmon mode p2 in (b).

Further, to gain computation time during the scattering electromagnetic problem we define the background field here fully analytically and plug it in a second step where we solve for the scattered field. Also, to study the modulation of plasmonic modes p1 and p2 seen in Fig. 1(c), we set the incidence angle of the incident field as $\theta \approx 51°$, and as pointed out already prior to the scattering study a moving mesh step is applied based on the SAW acoustic study realized before it. The max allowed displacement field set in/around the dimer is slightly scaled-up by a factor of $\sim$2.25 (comparing with Fig. 5) so that we get $u_{max} \approx 3.1$ nm i.e, a deformation rate of $\sim$ 1 %. This is done simply to get a better visibility of the dimer cross section spectra shift. We see that the scattering cross section spectrum (near the max) is clearly shifted as the phase of the acoustic compression mode is changed, showing the modulation of the plasmon. We note that the amount by which the plasmon is modulated between phases $\phi = 2$ $[rad]$ and 5 $[rad]$ is of $\delta\lambda_1 \sim$ 13.4 nm for plasmon mode p1 (Fig. 6(a)) and roughly of $\delta\lambda_2 \sim$ 6.57 nm for plasmon mode p2 (Fig. 6(b)). Note that these values reflect perfectly the applied scalability when making the comparison of these modulation wavelengths with respect to those computed earlier in Figs. 5(b)–5(c).

Optics EXPRESS

5. Conclusion

Thorough numerical calculations have been performed in this work to investigate the possibility of monitoring OMC using surface acoustic waves in a metal film-coupled nanoparticles system. The proposed design is made out of dimer gold ridges atop a metal plate deposited on SiO_2 substrate and covered with thin polymer film. We have first studied optical scattering properties of the dimer, and found three MIM-type localized plasmons in the frequency range of interest, namely the infrared domain. Such modes are strongly confined under the dimer or both under and in-between the ridges. In particular, the modes are shown to have narrower linewidths and higher scattering coefficients as compared to a monomer atop the structure. Furthermore, their behavior as function of the key geometrical parameters of the system analyzed numerically are successfully captured with a MIM-like effective cavity model. Acoustic study of the system shows that localized mechanical eigen-modes of the dimer arise out of the dimer mechanical coupling. Such modes falling at sub-GHz range are in-phase or out-of-phase flexural, compressional and higher order flexural modes. Optomechanical coupling of these modes with the MIM-strongly localized plasmons determined by optical modeling is analyzed through the computation of OMC coefficients g_{OM}. Regarding the dimer eigen-modes, it is found that in-phase compression mode yields a particularly higher g_{OM} for both considered plasmonic modes as it strongly deforms the MIM-like cavity under the dimer, while in-phase flexural mode shows a significant g_{OM} with a lesser magnitude.

Then, we have studied the effect of surface acoustic waves excited at the inlet of the structure. The interaction is analyzed through the transmission spectrum of the system showing the effective excitation of in/out of phase flexural and compressional modes. Observed dimer modes result from the splitting of the original monomer modes. Application of moving mesh enabled us to investigate OMC of compressional in-phase and flexural anti-phase dimer modes with the localized plasmons at $\sim$ 1638 *nm* and $\sim$ 926 *nm*. We find that in-phase compression mode strongly overlaps with plasmon p1 and slightly less with plasmon p2 as we observed a maximum modulation of the plasmon resonance wavelength of $\delta\lambda \sim$ 6.4 *nm* for mode p1 and $\delta\lambda \sim$ 2.7 *nm* for mode p2. Out-of-phase flexural mode yields a significant coupling for mode p1 with a modulation max of $\delta\lambda \sim$ 2.3 *nm* whilst plasmon mode p2 shows a weaker coupling.

We show that the optomechanically inactive monomer flexural mode becomes active due to dimer coupling, indicating a potential interest of dimers over monomers. While comparing the efficiency of the out-of-phase flexural mode and the in-phase compressional mode to modulate the dimer plasmonic modes, we noticed that the former has a weaker intrinsic OMC with respect to the latter, while the opposite situation occurs when the force creating the surface acoustic wave is fixed. This results from a stronger excitation of the flexural mode by the SAW than the compressional mode. Such findings based on the proposed SAW-dimer FCN design could lead to conception of nanoscale acousto-optic devices for light modulation in infrared, high frequency nanomechanical ultrasensitive sensors or biosensors and optical switches.

Funding. Agence Nationale de la Recherche (ANR-19-CE24-0014).

Acknowledgments. The author AN would like to thank Dr Abdellatif Gueddida for helpful discussions in order to complete this work.

Disclosures. The authors declare no conflicts of interest.

Data availability. No data were generated or analyzed in the presented research.

Supplemental document. See Supplement 1 for supporting content.

References

1. D. A. Fuhrmann, M. T. Susanna, H. kim, D. Bouwmeester, P. M. Petroff, A. Wixforth, and H. J. Krenner, "Dynamic modulation of photonic crystal nanocavities using gigahertz acoustic phonons," Nat. Photonics **5**(10), 605–609 (2011).

Optics EXPRESS

2. V. Laude, A. Belkhir, A. F. Alabiad, M. Addouche, S. Benchabane, A. Khelif, and F. I. Baida, "Extraordinary nonlinear transmission modulation in a doubly resonant acousto-optical structure," Optica **4**(10), 1245–1250 (2017).
3. M. Sansa, M. Defoort, A. Brenac, M. Sansa, M. Defoort, A. Brenac, M. Hermouet, L. Banniard, A. Fafin, M. Gely, C. Masselon, I. Favero, G. Jourdan, and S. Hentz, "Optomechanical mass spectrometry," Nat. Commun. **11**(1), 3781 (2020).
4. H. Xiong, L.-G. Si, and Y. Wu, "Precision measurement of electrical charges in an optomechanical system beyond linearized dynamics," Appl. Phys. Lett. **110**(17), 171102 (2017).
5. J. Xia, Q. Qiao, G. Zhou, F. S. Chau, and G. Zhou, "Opto-Mechanical Photonic Crystal Cavities for Sensing Application," Appl. Sci. **10**(20), 7080 (2020).
6. D. P. Lake, M. Mitchell, D. D. Sukachev, and P. E. Barclay, "Processing light with an optically tunable mechanical memory," Nat. Commun. **12**(1), 663 (2021).
7. H. Ren, M. H. Matheny, G. S. MacCabe, J. Luo, H. Pfeifer, M. Mirhosseini, and O. Painter, "Two-dimensional optomechanical crystal cavity with high quantum cooperativity," Nat. Commun. **11**(1), 3373 (2020).
8. W. Yang, S. A. Gerke, K. W. Ng, Y. Rao, C. Chase, and C. J. Chang-Hasnain, "Laser optomechanics," Sci. Rep. **5**(1), 13700 (2015).
9. D. Royer and E. Dieulesaint, "Elastic Waves in Solids," (Springer, New York, 2000).
10. C. Baker, W. Hease, D.-T. Nguyen, A. Andronico, S. Ducci, G. Leo, and I. Favero, "Photoelastic coupling in gallium arsenide optomechanical disk resonators," Opt. Express **22**(12), 14072–14086 (2014).
11. K. C. Balram, M. Davanço, J. Y. Lim, J. D. Song, and K. Srinivasan, "Moving boundary and photoelastic coupling in GaAs optomechanical resonators," Optica **1**(6), 414–420 (2014).
12. A. Yariv and P. Yeh, "Optical Waves in Crystals: Propagation and Control of Laser Radiation," John Wiley and Sons, New Jersey, (2003).
13. B. Djafari-Rouhani, S. El-Jallal, and Y. Pennec, "Phoxonic crystals and cavity optomechanics," C. R. Phys. **17**(5), 555–564 (2016).
14. M. H. Aram and S. Khorasani, "Optomechanical coupling strength in various triangular phoxonic crystal slab cavities," J. Opt. Soc. Am. B **35**(6), 1390–1396 (2018).
15. S. El-Jallal, M. Oudich, Y. Pennec, B. Djafari-Rouhani, A. Makhoute, Q. Rolland, S. Dupont, and J. Gazalet, "Optomechanical interactions in two-dimensional Si and GaAs phoXonic cavities," J. Phys.: Condens. Matter **26**(1), 015005 (2014).
16. J. Chan, A. H. Safavi-Naeini, J. T. Hill, S. Meenehan, and O. Painter, "Optimized optomechanical crystal cavity with acoustic radiation shield," Appl. Phys. Lett. **101**(8), 081115 (2012).
17. M. Oudich, S. El-Jallal, Y. Pennec, B. Djafari-Rouhani, J. Gomis-Bresco, D. Navarro-Urrios, C. M. Sotomayor Torres, A. Martıinez, and A. Makhoute, "Optomechanic interaction in a corrugated phoxonic nanobeam cavity," Phys. Rev. B **89**(24), 245122 (2014).
18. J. Gomis-Bresco, D. Navarro-Urrios, M. Oudich, S. El-Jallal, A. Griol, D. Puerto, E. Chavez, Y. Pennec, B. Djafari-Rouhani, F. Alzina, A. Martınez, and C. M. Sotomayor Torres, "A one-dimensional optomechanical crystal with a complete phononic band gap," Nat. Commun. **5**(1), 4452 (2014).
19. T.-R. Lin, Y.-C. Huang, and J.-C. Hsu, "Optomechanical coupling in phoxonic–plasmonic slab cavities with periodic metal strips," J. Appl. Phys. **117**(17), 173105 (2015).
20. A. Girard, H. Gehan, A. Mermet, C. Bonnet, J. Lermé, A. Berthelot, E. Cottancin, A. Crut, and J. Margueritat, "Acoustic mode hybridization in a single dimer of gold nanoparticles," Nano Lett. **18**(6), 3800–3806 (2018).
21. A. Girard, J. Lermé, H. Gehan, A. A. Mermet, C. Bonnet, E. Cottancin, A. Crut, and J. Margueritat, "Inelastic light scattering by multiple vibrational modes in individual gold nanodimers," J. Phys. Chem. C **123**(23), 14834–14841 (2019).
22. A. Noual, E. Kang, T. Maji, M. Gkikas, B. Djafari-Rouhani, and G. Fytas, "Optomechanic Coupling in Ag Polymer Nanocomposite Films," J. Phys. Chem. C **125**(27), 14854–14864 (2021).
23. C. Voisin, N. Del Fatti, D. Christofilos, and F. Vallee, "Time-resolved investigation of the vibrational dynamics of metal nanoparticles," Appl. Surf. Sci. **164**(1-4), 131–139 (2000).
24. G. Soavi, I. Tempra, M. F. Pantano, A. Cattoni, S. Collin, P. Biagioni, N. M. Pugno, and G. Cerullo, "Ultrasensitive Characterization of Mechanical Oscillations and Plasmon Energy Shift in Gold Nanorods," ACS Nano **10**(2), 2251–2258 (2016).
25. P.-A. Mante, L. Belliard, and B. Perrin, "Acoustic phonons in nanowires probed by ultrafast pump-probe spectroscopy," Nanophotonics **7**(11), 1759–1780 (2018).
26. C. Lumdee, B. Yun, and P. G. Kik, "Effect of surface roughness on substrate-tuned gold nanoparticle gap plasmon resonances," Nanoscale **7**(9), 4250–4255 (2015).
27. G.-C. Li, Q. Zhang, S. A. Maier, and D. Lei, "Plasmonic particle-on-film nanocavities: a versatile platform for plasmon-enhanced spectroscopy and photochemistry," Nanophotonics **7**(12), 1865–1889 (2018).
28. G.-C. Li, Y.-L. Zhang, and D. Y. Lei, "Hybrid plasmonic gap modes in metal film-coupled dimers and their physical origins revealed by polarization resolved dark field spectroscopy," Nanoscale **8**(13), 7119–7126 (2016).
29. R. T. Hill, J. J Mock, A. Hucknall, S. D. Wolter, N. M. Jokerst, D. R. Smith, and A. Chilkoti, "Plasmon ruler with angstrom length resolution," ACS Nano **6**(10), 9237–9246 (2012).
30. C. Ciraci, R. T. Hill, J. J. Mock, Y. Urzhumov, A. I. Fernandez-Dominguez, S. A. Maier, J. B. Pendry, A. Chilkoti, and D. R. Smith, "Probing the Ultimate Limits of Plasmonic Enhancement," Science **337**(6098), 1072–1074 (2012).

Optics EXPRESS

31. G. Hajisalem, M. S. Nezami, and R. Gordon, "Probing the Quantum Tunneling Limit of Plasmonic Enhancement by Third Harmonic Generation," Nano Lett. **14**(11), 6651–6654 (2014).
32. R. Thijssen, E. Verhagen, T. J. Kippenberg, A. Polman, and N. Lett, "Plasmon Nanomechanical Coupling for Nanoscale Transduction," Nano Lett. **13**(7), 3293–3297 (2013).
33. R. Thijssen, T. J. Kippenberg, A. Polman, E. Verhagen, and N. Lett, "Plasmomechanical resonators based on dimer nano-antennas," Nano Lett. **15**(6), 3971–3976 (2015).
34. Z. Oumekloul, M. Moutaouekkil, G. Lévêque, A. Talbi, A. Mir, and A. Akjouj, "Nanomechanical modulation cavities of localized surface plasmon resonance with elastic whispering-gallery modes," J. Appl. Phys. **127**(2), 023105 (2020).
35. W. M. Deacon, A. Lombardi, F. Benz, Y. D. V.-I. Redondo, R. Chikkaraddy, B. D. Nijs, M.-E. Kleemann, J. Mertens, and J. J. Baumberg, "Interrogating Nanojunctions Using Ultraconfined Acoustoplasmonic Coupling," Phys. Rev. Lett. **119**(2), 023901 (2017).
36. Y. Wang, Z. Li, K. Zhao, A. Sobhani, X. Zhu, Z. Fang, and N. J. Halas, "Substrate-mediated charge transfer plasmons in simple and complex nanoparticle clusters," Nanoscale **5**(20), 9897–9901 (2013).
37. H. Liu, J. Ng, S. B. Wang, Z. H. Hang, C. T. Chan, and S. N. Zhu, "Strong plasmon coupling between two gold nanospheres on a gold slab," New J. Phys. **13**(7), 073040 (2011).
38. A. Mrabti, G. Lévêque, A. Akjouj, Y. Pennec, B. Djafari-Rouhani, R. Nicolas, T. Maurer, and P. M. Adam, "Elastoplasmonic interaction in metal-insulator-metal localized surface plasmon systems," Phys. Rev. B **94**(7), 075405 (2016).
39. M. Hu and F. L. Duan, "Design, fabrication and characterization of SAW devices on LiNbO3 bulk and ZnO thin film substrates," Solid-State Electron. **150**, 28–34 (2018).
40. J. Mei, N. Zhang, and J. Friend, "Fabrication of Surface Acoustic Wave Devices on Lithium Niobate," J. Visualized Exp. **160**, e61013 (2020)..
41. R. Salenbien, R. Côte, J. Goossens, P. Limaye, R. Labie, and C. Glorieux, "Laser-based surface acoustic wave dispersion spectroscopy for extraction of thicknesses, depth, and elastic parameters of a subsurface layer: Feasibility study on intermetallic layer structure in integrated circuit solder joint," J. Appl. Phys. **109**(9), 093104 (2011).
42. A. Okada, F. Oguro, A. Noguchi, Y. Tabuchi, R. Yamazaki, K. Usami, and Y. Nakamura, "Cavity Enhancement of Anti-Stokes Scattering via Optomechanical Coupling with Surface Acoustic Waves," Phys. Rev. Appl. **10**(2), 024002 (2018).
43. K. C. Balram, M. I. Davanço, J. D. Song, and K. Srinivasan, "Coherent coupling between radiofrequency, optical and acoustic waves in piezo-optomechanical circuits," Nat. Photonics **10**(5), 346–352 (2016).
44. T.-R. Lin, C.-H. Lin, and J.-C. Hsu, "Strong Optomechanical Interaction in Hybrid Plasmonic-Photonic Crystal Nanocavities with Surface Acoustic Waves," Sci. Rep. **5**(1), 13782 (2015).
45. A. V. Korovin, Y. Pennec, M. Stocchi, D. Mencarelli, L. Pierantoni, T. Makkonen, J. Ahopelto, and B. Djafari-Rouhani, "Conversion between surface acoustic waves and guided modes of a quasi-periodic structured nanobeam," J. Phys. D: Appl. Phys. **52**(32), 32LT01 (2019).
46. A. Noual, R. Akiki, Y. Pennec, E. H. El Boudouti, and B. Djafari-Rouhani, "Surface Acoustic Waves-Localized Plasmon Interaction in Pillared Phononic Crystals," Phys. Rev. Appl. **13**(2), 024077 (2020).
47. A. Crut, P. Maioli, N. Del Fatti, and F. Vallée, "Acoustic vibrations of metal nano-objects: Time-domain investigations," Phys. Rep. **549**, 1–43 (2015).
48. C. Yi, P. D. Dongare, M.-N. Su, W. Wang, D. Chakraborty, F. Wen, W.-S. Chang, J. E. Sader, P. Nordlander, N. J. Halas, and S. Link, "Vibrational coupling in plasmonic molecules," Proc. Natl. Acad. Sci. U. S. A. **114**(44), 11621–11626 (2017).
49. M. Li, H. X. Tang, and M. L. Roukes, "Ultra-sensitive NEMS-based cantilevers for sensing, scanned probe and very high-frequency applications," Nat. Nanotechnol. **2**(2), 114–120 (2007).
50. Z. Wang, Q. Wang, W. Zhang, H. Wei, Y. Li, and W. Ren, "Ultrasensitive photoacoustic detection in a high-finesse cavity with Pound–Drever–Hall locking," Opt. Lett. **44**(8), 1924 (2019).
51. P. J. M. van der Slot, M. A. G. Porcel, and K. J. Boller, "Surface acoustic waves for acousto-optic modulation in buried silicon nitride waveguides," Opt. Express **27**(2), 1433 (2019).
52. P. Roelli, C. Galland, N. Piro, and T. J. Kippenberg, "Molecular cavity optomechanics as a theory of plasmon-enhanced Raman scattering," Nat. Nanotechnol. **11**(2), 164–169 (2016).
53. X. Wang, S.-C. Huang, S. Hu, S. Yan, and B. Ren, "Fundamental understanding and applications of plasmon-enhanced Raman spectroscopy," Nat. Rev. Phys. **2**(5), 253–271 (2020).
54. C. Zhang, T. Zhang, Z. Zhang, and H. Zheng, "Plasmon Enhanced Fluorescence and Raman Scattering by [Au-Ag Alloy NP Cluster] @SiO_2 Core-Shell Nanostructure," Front. Chem. **7**, 647 (2019).
55. A. Raman and S. Fan, "Photonic Band Structure of Dispersive Metamaterials Formulated as a Hermitian Eigenvalue Problem," Phys. Rev. Lett. **104**(8), 087401 (2010).
56. N. W. Ashcroft and D. N. Mermin, "Solid State Physics," (Brooks Cole, Belmont, CA, 1976).
57. W. Yan, R. Faggiani, and P. Lalanne, "Rigorous modal analysis of plasmonic nanoresonators," Phys. Rev. B **97**(20), 205422 (2018).
58. J. Dorfmüller, R. Vogelgesang, R. T. Weitz, C. Rockstuhl, C. Etrich, T. Pertsch, F. Lederer, and K. Kern, "Fabry-Pérot Resonances in One-Dimensional Plasmonic Nanostructures," Nano Lett. **9**(6), 2372–2377 (2009).
59. S. Jia, Y. Wu, X. Wang, and N. Wang, "A Subwavelength Focusing Structure Composite of Nanoscale Metallic Slits Array With Patterned Dielectric Substrate," IEEE Photonics J. **6**(1), 1–8 (2014).

Optics EXPRESS

60. S. G. Johnson, M. Ibanescu, A. Skorobogatiy, O. Weisberg, J. D. Joannopoulos, and Y. Fink, "Perturbation theory for Maxwell's equations with shifting material boundaries," Phys. Rev. E **65**(6), 066611 (2002).
61. A. Ahmed, M. Pelton, and J. R. Guest, "Understanding how acoustic vibrations modulate the optical response of plasmonic metal nanoparticles," ACS Nano **11**(9), 9360–9369 (2017).
62. O. Saison-Francioso, G. Lévêque, and A. Akjouj, "Numerical modeling of acousto–plasmonic coupling in metallic nanoparticles," J. Phys. Chem. C **124**(22), 12120–12133 (2020).
63. N. Hooshmand and M. A. El-Sayed, "Collective multipole oscillations direct the plasmonic coupling at the nanojunction interfaces," Proc. Natl. Acad. Sci. U. S. A. **116**(39), 19299–19304 (2019).